Continental records of organic carbon isotopic composition (δ13Corg), weathering, paleoclimate and wildfire linked to the End-Permian Mass Extinction

Lu, Jing; Zhang, Peixin; Yang, Minfang; Shao, Longyi; Hilton, Jason

Continental records of organic carbon isotopic composition ($\delta^{13}C_{org}$), weathering, paleoclimate and wildfire linked to the End-Permian Mass Extinction

Jing LU[a]*, Peixin ZHANG[a], Minfang YANG[b], Longyi SHAO[a], Jason HILTON[c]

[a] *State Key Laboratory of Coal Resources and Safe Mining, College of Geoscience and Surveying Engineering, China University of Mining and Technology, Beijing 100083, PR China*

[b] *Petroleum Exploration and Development Research Institute, PetroChina, Beijing100083, PR China*

[c] *School of Geography, Earth and Environmental Sciences, The University of Birmingham, Edgbaston, Birmingham B15 2TT, UK*

* Corresponding author at: State Key Laboratory of Coal Resources and Safe Mining, College of Geoscience and Surveying Engineering, China University of Mining and Technology, Beijing 100083, P. R. China

E-mail address: *lujing@cumtb.edu.cn*

ABSTRACT

The late Permian was the acme of Pangea assembly, with collision and subduction of global plates accompanied by major changes in atmospheric composition, paleoclimates and paleoenvironments of the Earth's surface system. These events are extensively recorded in marine successions from the Tethys, but much less are known from continental successions that typically lack high-resolution stratigraphic control. In order to reveal these fluctuations in terrestrial strata and their relationship with the End-Permian Mass Extinction (EPME), we investigate continental $\delta^{13}C_{org}$, mercury and nickel concentrations, wildfire, and climate change proxies from the late Permian Changhsingian stage to Early Triassic Induan stage in the Yuzhou coalfield in the North China Plate (NCP). Results show two negative organic carbon isotope excursions (CIE) within the Changhsingian aged Sunjiagou Formation, the first (CIE-I, 2.2‰) during mid-Changhsingian and a second, larger, excursion (CIE-II, 2.7‰) near the end of the Changhsingian that coincides with the peaks in the Chemical Index of Alteration (CIA) value and extinction of plant species. We infer CIE-II to be the global negative excursion of $\delta^{13}C_{org}$ associated with the EPME. Arid climates prevailed in the study area from the Changhsingian to the early Induan inferred from the low kaolinite contents and weak continental weathering, except for two short-duration episodes with higher humidity that correspond with CIE-I and CIE-II. Extremely high fusinite content ($\bar{x}$ = 63.1%) and its increasing abundance through the Changhsingian indicates that frequent wildfires may have been a direct cause for both the destruction of terrestrial vegetation ecosystems and the rapid decline of terrestrial biodiversity at the EPME. We consider that terrestrial ecosystems may have played an important role in the extinction of marine communities at the EPME. This represents the first time the EMPE has been demonstrated in the NCP based on combined evidence from negative carbon isotope excursion, concurrent weathering trends, Ni/Al ratio and biotic extinctions, representing an important step in accurately identifying and correlating the EPME in continental settings from the NCP.

Keywords: terrestrial strata, organic carbon isotope composition, weathering, palaeoclimate, wildfire, End-Permian Mass Extinction, North China Plate

1. Introduction

The End-Permian Mass Extinction (EPME) represents the largest mass extinction event in Earth history, and resulted in substantial loss of 90% marine and 70% terrestrial species (Erwin, 1994). The extinction was related to extreme fluctuations in atmospheric composition, paleoclimates and paleoenvironments on the Earth's surface system, that included rapid and sustained global warming (Joachimski et al., 2012; Sun et al., 2012), ocean anoxia (Wignall and Twitchett, 1996) and widespread wildfires (Shen et al., 2011; Chu et al., 2020) amongst other kill mechanisms (Bond and Grasby, 2017). Although the underlying triggers and extinction mechanisms for the EPME are complex and difficult to disentangle from each other (Bond and Grasby, 2017; Wignall et al., 2020), it is generally considered that the deterioration of global climate and environment is related to intense volcanic activity from the Siberian Traps during the Permian–Triassic (P–T) transition (Shen et al., 2011; Burgess and Bowring, 2015; Ernst and Youbi, 2017).

Studies linking the EPME to changes in global climate and environment primarily focus on marine strata (Wignall and Hallam, 1992; Wignall and Twitchett, 1996; Grasby and Beauchamp, 2009; Shen et al., 2011, 2013; Grasby et al., 2013, 2016; Liao et al., 2016, 2020) due to their often continuous deposition and well-dated stratigraphic frameworks. By contrast, fewer studies have focused on contemporaneous continental conditions despite their obvious link to the EPME as a major source of nutrients flushed into marine settings (Algeo et al., 2013; Wignall et al., 2020). At the same time ocean hypoxia thought to be triggered by algal and cyanobacterial proliferation in surface waters is a common phenomenon accompanied by the extinction of marine life (e.g., Xie, 2007). However, the reason for cyanobacterial proliferation is controversial. Some studies have attributed it to increased terrestrial input of nutrients caused by enhanced continental weathering (e.g., Algeo and Twitchett, 2010) with post-EPME oceans having high bioproductivity (e.g., Meyer, 2011; Shen et al., 2015). In contrast, other studies consider it may result from the transformation of nitrogen into ammonium in anoxic environments (Sun et al., 2019), with the role of land-sourced nutrients limited and oceanic primary productivity low (Grasby et al., 2016a, 2019a; Sun et al., 2019). Therefore, contemporaneous continental strata are important to understand the relationship of climate, weathering and environmental changes between continents and marine settings.

From the P–T transition interval in the NCP, numerous past studies have focused on stratigraphy, sedimentology, palaeontology and tectonics (e.g., Wang and Wang, 1986; Hou and Ouyang, 2000; Chu et al., 2015, 2017, 2019; Zhao et al., 2017), making these continental strata ideal for evaluating climate and environmental changes during this time period. These have identified major changes in terrestrial diversity including extinctions in conchostracans and ostracoda (Chu et al., 2015), as well as a dramatic reduction in plant species diversity near the boundary of the Changshingian aged Sunjiagou Formation and Induan aged Liujiagou Formation (Chu et al., 2015, 2019). In recent years, elevated mercury and nickel levels as a signature for volcanism have been documented in marine and terrestrial sediments associated with the EPME (Sanei et al., 2012; Grasby et al., 2013, 2015, 2016b; 2019b; Burgess and Bowring, 2015; Rampino et al., 2017; Fielding et al., 2019; Shen J et al., 2019; Chu et al., 2020), but elevated mercury and nickel levels have not previously been recorded in the continental environments of the NCP.

Using the ZK21-1 borehole core in the Yuzhou Coalfield of the southern NCP, we consider fluctuations in $\delta^{13}C_{org}$, mercury and nickel concentrations, clay mineral components, Mineralogical Index of Alteration (MIA) for sandstones, the Chemical Index of Alteration (CIA) for mudstones, and kerogen macerals to evaluate the changes of global carbon cycle, volcanism, climate, continental weathering trend and wildfires in relation to the EPME. This represents an important step in the application of these proxies to evaluate the Permian-Triassic boundary interval in the continental successions of the NCP.

2. Geological background

During early Lopingian period, the NCP, surrounded by the Inner Mongolia uplift (IMU) to the north and the North Qinling Belt (NQB, or Funiu paleo-land) to the south, was located in the northeastern margin of the Paleo-Tethys Ocean (Fig. 1a), with a latitude of approximately 20° N (Ziegler et al., 1997; Shang, 1997; Li, 2006; Muttoni et al., 2009). It was separated from the South China Plate by the Paleo-Tethys Ocean, and from the Mongolian plate by the paleo-Asian ocean (Zhao et al., 2017; Fig. 1a, e). During this period, sediments were mainly sourced from the northern IMU for the ongoing southward subduction of the paleo-Asian Ocean beneath the NCP (Zhang et al., 2014). In the Changhsingian stage, the NQB begin to uplift and became the secondary provenance of the NCP, but the main provenance for the study area in the Yuzhou coalfield located in the southern NCP (Shang, 1997). The main part of the NQB is represented by the Qinling Group consisting predominantly of Precambrian basement units including gneiss and amphibolite (Zhang et al., 1995; Dong and Santosh, 2016).

The stratigraphic succession, rock types and fossil plant assemblages from the late Permian to Early Triassic in the study area are shown in Figure 2. The strata studied in this paper conformably overlie the Upper Shihezi Formation and comprise the Sunjiagou Formation and the lower part of the overlying Liujiagou Formation. The Sunjiagou Formation has been divided into three members according to their lithological association (Yang and Lei, 1987; Wang, 1997). The lower and middle members of the Sunjiagou Formation are composed of medium-coarse, feldspathic quartz sandstone and thin layers of siltstone and mudstone, while the upper part of the Sunjiagou Formation is composed only of thin layers of mudstone and siltstone, all deposited in a shore-shallow lake environment (Guo et al., 1991). Based on sporo-pollen and plant fossil assemblages, previous studies have assigned the Sunjiagou Formation to the Changhsingian stage, and the conformably overlying Liujiagou Formation to the early Early Triassic Induan stage (Wang and Wang, 1986; Hou and Ouyang, 2000; Wang and Chen, 2001; Chu et al., 2015). The Liujiagou Formation mainly encompasses thickly layered medium to coarse sandstone, fine-grained sandstones and siltstones with few trace fossils, mainly deposited in a braided river sedimentary system. The base of its lowermost Jindoushan Sandstone member has been regarded as a regional marker for the Permian-Triassic boundary (Guo et al., 1991; Fig. 2d). Within the Yuzhou Coalfield, we studied borehole ZK21-1 that lies within the Putaosi exploration area that is a monoclinal structure inclined toward the southwest (Fig. 1b, c, d).

3. Materials and methods

From the ZK21-1 borehole in the Yuzhou coalfield, fresh sandstone (27 samples) and mudstone (22 samples), were collected from the Sunjiagou Formation to the lower part of the Liujiagou Formation. Sampling locations are shown in Figure 3. Every mudstone sample was first broken down to less than 1 mm and then divided into two parts. One part was prepared for kerogen enrichment and identification according to the China national standard (SY/T5125-2014), with no less than 300 effective points per sample analyzed. The remaining part of each mudstone sample was further crushed below 200 mesh and divided into six subparts for (1) $\delta^{13}C_{org}$ analysis, (2) clay mineral analysis, (3) Total organic content (TOC) analysis, (4) major elements analysis, (5) trace elements analysis, and (6) mercury concentration analysis. Clay mineral and mercury concentration were measured at the State Key Laboratory Coal Resources and Safe Mining (Beijing), and the other analyses in Beijing Research Institute of Uranium Geology.

Organic carbon isotope analysis was performed using a stable isotope mass spectrometer (MAT253), and $\delta^{13}C_{org}$ values are expressed in per mil (‰) with respect to the Vienna Pee Dee Belemnite (VPDB) standard, with the absolute analysis error of ±0.1‰. Clay mineral was analyzed using an X-ray diffractometer (D/max 2500 PC), and the data were interpreted using Clayquan 2016 software with the relative analysis error of ±5%. Samples for TOC were first treated with phosphoric acid to remove inorganic carbon, and then the TOC values were measured using a carbon-sulfur analyzer (CS580-A) with the lower detection limits of 100 μg/g and the absolute analysis error of ±0.2%. Major elements analysis was undertaken with an X-ray fluorescence spectrometer (PW2404) with the relative analysis error of ±5%. Trace elements analysis was undertaken using an inductively coupled plasma mass spectrometer (Finnigan MAT) with the relative analysis error better than ±5%. Mercury concentration was undertaken using a mercury analyzer (Lumex RA-915+) with lower detection limits of 2ng/g and the relative analysis error of ±5%. More details of the analytical method are described by Ma et al. (2015), Liao et al. (2016), Wu et al. (2017), Hu et al. (2020) and Chu et al. (2020). Sandstone samples were cut into slices and identified by the point-counting method under a microscope with more than 300 effective points of each sample. The classification of sandstone components is in accordance with that of Dickinson (1985).

In this study, mercury and nickel concentrations have been used to indicate the presence of volcanic activity due to their relationship with volcanic eruptions and magmatic intrusions (Sanei et al., 2012; Burgess and Bowring, 2015; Rampino et al., 2017; Grasby et al., 2019b).The indexes of MIA of sandstone and CIA of mudstone were used to restore the weathering trends of the parent rock in provenance, their concepts and implications are outlined by Nesbitt and Young (1984), Fedo et al. (1995), and Roy and Roser (2013). Paleoclimate inferences have been recovered by the kaolinite content of mudstone, with MIA and CIA values used for reference. As the abundance of kaolinite in modern sediments is dependent on the intensity of chemical weathering controlled by climate (Chamley, 1989), and because of its strong diagenesis resistance, changes in its content are considered to be a reliable climatic proxy (Thiry, 2000). Fusinite (Charcoal) content has been used to indicate paleowildfire (e.g., Scott, 2000; Glasspool and Scott, 2010).

4. Results

4.1. Total organic content (TOC) and distribution pattern of $\delta^{13}C_{org}$

Results for TOC and $\delta^{13}C_{org}$ are shown in Table 1 and Figure 3a, b. TOC values vary from 0.05–

0.12 % (x̄ = 0.09%). These values are low 0.2% detection limit (see Grasby et al., 2019b) and will not be used in the following discussion.

$\delta^{13}C_{org}$ values vary from -26.5–23.0 ‰ (x̄ = -24.7‰), and show a vertical variation trend from fast negative excursion with an offset of 2.2‰ (CIE-I) in the middle of the Sunjiagou Formation, followed by slow positive excursion with an offset of 1.4‰. Near the top of the Sunjiagou Formation, a second, larger excursion occurs with an offset of 2.7‰ (CIE-II). After CIE-II, $\delta^{13}C_{org}$ values increase at the base of the Liujiagou Formation (Fig. 3b). Vertically, CIE-I and CIE-II corresponds approximately with the position of the two zones of high TOC values (Fig. 3a). High TOC values occur elsewhere in the succession without corresponding $\delta^{13}C_{org}$ excursions (Fig. 3a, b).

4.2. Mercury and Nickel concentration

Results for mercury and nickel concentrations are shown in Table 1. Hg concentrations vary from 2.21–27.04 ng/g (x̄ = 22.5 ng/g) (Table. 1) with an obvious peak in Hg concentration corresponding to the position of CIE-II. Although the peak value in Hg concentration is 3 times the average concentration, the value of Hg concentrations are within the average values of marine shale in published papers (c.f. Grasby et al., 2019b). The nature of the Hg peak is not clear and we do not regard it as definitive evidence for volcanism in the study area.

Nickel concentrations vary from 21.5–69.7 μg/g (x̄ = 34.45 μg/g) with an obvious peak in concentration corresponding to the position of CIE-II. The value of the peak (69.7 μg/g) is within the range recorded during the P-T transition (12-800μg/g; see Ramponi et al., 2017 and references therein).

Although Ni concentration may be related to volcanism, some researchers consider it to be influenced by aluminium content (e.g., Fielding et al., 2019). We corrected Ni concentrations by aluminium concentration and the values of the Ni/Al ratio (Fig. 3e) vary from 2.36–6.72 $\times 10^{-4}$ (x̄ = 3.87×10^{-4}). Two peaks in Ni/Al ratio occur of which the lower one is coincident with the position of

CIE-II (Fig. 3b), indicating that the peak in Ni concentration and Ni/Al ratio corresponding to CIE-II is reasonable to be inferred as evidence of volcanism affecting the study area.

4.3. Kerogen macerals

Identification results of kerogen macerals are shown in Table 1 and Figure 3f. Inertinite content varies from 49.3–70.1 % ($\bar{x}$ = 63.1%) and entirely comprises fusinite (charcoal) which is opaque, pure black, does not fluoresce under fluorescence illumination (Fig. 4a-c) and is usually long and thin or fragmental shaped with sharp edges. Vertically through the succession, fusinite concentration increases slowly at first, reaches a peak value of 70.1% near the top of the Sunjiagou Formation, and then decreases slowly after entering the Liujiagou Formation. The vitrinite group, with contents varying from 24.4–45.0 % ($\bar{x}$ = 29.0%) mainly comprises normal vitrinite (Fig. 4d, e). Exinite content varies from 3.6–11.9 % ($\bar{x}$ = 7.7%) of which suberinite is the main component (Fig. 4f, g). Sapropelinite content is very low with an average value of 0.3% (Fig. 4h-k).

4.4. MIA, CIA, and Clay mineral component

The values of the Th/U ratio vary from 2.04 – 4.92 (Table 3), indicating that the parent rocks of the sediments in the study area are not recycled. This is because recycled mudrocks exhibit high Th/U ratios of around 6 due to oxidation of U^{4+} to U^{6+} and its removal as a soluble component (c.f. Bhatia and Taylor, 1981). This conclusion is consistent with the provenance properties (stable land) indicated by the Dickson diagram (Fig. 5a) and is in agreement with Shang (1997) and Dong and Santosh (2016) who determined sediments of the study area mainly originated from the North Qinling Terrane (NQT) based on paleogeographic restoration and lithofacies analysis.

A reliability test of the CIA values in the study area was undertaken by the A-CN-K diagram (Nesbitt and Young, 1984) that shows the CIA values deviate from the ideal weathering trend line (Fig. 5b) and are affected by potassium metasomatism. Subsequently, these CIA values were calibrated by the method of Fedo et al. (1995). MIA values vary from 70.9–91.8 ($\bar{x}$=78.8) (Table 2, Fig. 3g), most of which are between 70–80 and show a relatively stable vertical distribution through the succession, except for two intervals with MIA values > 80 near the middle of the Sunjiagou Formation and at the boundary of the Sunjiagou and Liujiagou formations. The corrected values (CIA_{corr}) vary from 78.1–86.5 ($\bar{x}$=83.7) (Table 3, Fig. 3h) and are similar to the MIA results, reflecting moderate weathering of source area and showing a similar vertical change pattern. This shows MIA and CIA are reliable indexes for indicating weathering trends in the study area. The two periods of enhanced weathering approximately correspond with negative excursions CIE-I and CIE-II (Fig. 3b, g, h).

The clay mineral components of the mudstone samples are mainly illite-smectite mixed layers, followed by kaolinite and illite (Table 3, Fig. 3i, 6). The content of illite-smectite mixed layers varies from 79–96 % ($\bar{x}$ = 90.5%). Kaolinite content changes from 2–18 % ($\bar{x}$ = 5.8%) and presents a vertical trend of first decreasing and then increasing, but with two peaks in kaolinite content (about 10% and 18%, respectively) corresponding roughly with the position of CIE-I and CIE-II. The illite content is very low with an average of 3.8%.

5. Discussion

5.1. Stratigraphic correlation and the position of the EPME

Previous studies of continental weathering in the Yima and Shichuanhe sections in the NCP during the P-T transition shown that CIA values tends to increase first and then decrease, with the maximum CIA values occurring at the top of the Sunjiagou Formation and approximately correspond to the End-Permian Plant Extinction (EPPE) (Cao et al., 2019). This provide a timeline for the position of the EPPE in the NCP. We follow this conclusion, using the peak in CIA as a marker for the EPPE and place the EPPE at the horizon coincident with CIE-II in the study area.

Furthermore, chemostratigraphy can provide evidence for the correlation between the EPPE in NCP and marine settings. Investigations on $\delta^{13}C$ distribution patterns from stratigraphically well-constrained Lopingian to early Triassic profiles have been undertaken in marine (Meishan, Niushan) (e.g., Shen et al., 2013; Liao et al., 2016, 2020) and terrestrial (Dalongkou, Lubei, Guanbachong, Chahe, Longmendong, Bunnerong-1) strata (e.g., Zhang et al., 2016; Shen J et al., 2019; Fielding et al., 2019). These reveal $\delta^{13}C$ is relatively stable during the early Changhsingian, followed by a gradual and slow decrease during the late Changhsingian prior to a globally significant excursion with an average negative offset of 3–5 ‰ shortly before the P–T boundary (Shen S et al., 2019). The end-Changhsingian negative excursion of $\delta^{13}C$ represents a major reorganization of the global carbon cycle associated with the EPME interval and is a global phenomenon (Shen S et al., 2011, 2013, 2019).

In the study area, the $\delta^{13}C_{org}$ trend is very similar to that in Meishan Changhsingian stratotype section at Changxing, South China (Nan and Liu, 2004). CIE-I occurs in mudstones on top of the Pingdingshan Sandstone (Fig. 3), it may be a regional negative excursion as while it is present in the Meishan section in South China, it is absent in many other sections globally (e.g., Yin et al., 2007). In our study, no changes in plant species composition occur at this level (Fig. 2h). CIE-II occurs near the top of the Sunjiagou Formation, and coincident it is a significant floral extinction event just below the P-T boundary (Fig. 2h) that occurs across the NCP (Wang and Wang, 1986; Chu et al., 2015). Moreover, peaks in nickel concentration and Ni/Al ratio during the P-T transition period also are within the extinction interval of the EPME (Rampino et al., 2017 and references therein; Fielding et al., 2019). As a result, we interpret CIE-II as correlating with the end-Changhsingian negative excursion associated with the EPME in Meishan Changhsingian stratotype section. Our study support the hypothesis that the extinction is synchronous in both terrestrial and marine successions (Shen S et al., 2011, 2013, 2019; Zhang et al., 2016) although other recent research shows that the extinction of terrestrial life earlier than that of marine life (Fielding et al., 2019; Gastaldo et al., 2020;

Chu et al., 2020). This might suggest that the terrestrial extinction was not synchronous, occurring earlier at higher latitudes and closer or at the same time as the marine extinction at lower latitudes (Feng et al., 2020).

5.2. Paleoclimate changes and continental weathering regimes

In the NCP during the Changhsingian, previous studies considered that arid paleoclimates prevailed (Yang and Lei, 1987; Cope et al., 2005; Yang and Wang, 2012), related to the northward drift of the NCP through arid subtropical latitudes and/or rain-shadow effect from topography resulting from collision with the Mongolia block (Cope et al., 2005). In study area, the wetland Cathaysian flora was rapidly succeeded by a Zechstein-type drier flora at the end of the Wuchiapingian (Yang and Wang, 2012; Fig. 2g). In the NCP, the absence of coal deposition, widespread distribution of red beds in the Sunjiagou and Liujiagou formations, and the occurrence of calcareous nodules in the upper part of Sunjiagou Formation collectively indicate high evaporation and an arid paleoclimate (Yang and Lei, 1987; Wang, 1997).

In our study a generally arid paleoclimate is evidenced based on low kaolinite content in mudstones and the moderate-weak continental weathering of the source area (Fig. 3g, h, i, 7a). However, this was not continuous with two short duration periods of relative humidity appearing in the mid-Changhsingian and near the P–T boundary (Fig. 7h). This is more pronounced in the latter event that coincides with CIE-II where kaolinite content of mudstones reaches 18%, and the values of MIA and CIA exceed 80 and 85, respectively. This conclusion is supported by records from the Yima and Shichuanhe sections in the NCP near the P–T boundary (Cao et al., 2019), where peaks in CIA values roughly correspond to the EPPE. At the same time, similar peaks in CIA values and Kaolinite content also were recorded in southeast Australia, the reason of which has been attributed to the intensification of humidity/warmth around the EPME (Fielding et al., 2019). Short-term climatic humidification and enhanced continental weathering in the P-T transition has also been recorded in other areas of the world (e.g., Bachmann and Kozur, 2004; Sheldon, 2005; Retallack, 2005; Song, 2015).

There is no consensus on whether or why the climate became wet near the P–T boundary. Many previous studies suggested that paleoclimate humification around the Tethys Ocean may be related to the increased precipitation and surface runoff caused by the intensification of Monsoon activity (Winguth and Winguth, 2013), or acceleration of the land water cycle caused by the rising global temperature (Van Soelen et al., 2018). However, some studies suggest that the increase of kaolinite content and the enhancement of continental weathering from the late Changhsingian to early Induan are related to the increase of atmospheric pCO_2 and acid rain caused by frequent volcanic activity (Algeo and Twitchett, 2010; Sun et al., 2018; Cao et al., 2019). This is because elevated acidity and temperature conditions can accelerate rock weathering rates. As such volcanic activity may mislead the paleoclimate and continental weathering trends based on kaolinite content as well as influencing MIA and CIA values.

In the study area, the increased kaolinite content and MIA and CIA values after the EPME occurred in a period of rapidly rising global sea level (Cao et al., 2009; Yin and Song, 2013). This significantly increased water vapor transportation to land (Winguth and Winguth, 2013), resulting in continental climatic humidification. This may explain the terrestrial climate wetting after the EPME but it cannot rule out the possibility that climate humidification and the prevalence of acid rain occurred simultaneously.

5.3. Continental Wild-fire linked to EPME and marine extinctions

Fusinite, or charcoal, is fire-derived and evidences wildfires in the rock record (Scott, 2000; Glasspool and Scott, 2010). In the Yuzhou coalfield, inertinite (fusinite) is the most abundant kerogen maceral group ($\bar{x}$ = 63.1%). The high fusinite content and its vertical variation pattern (see 4.3) indicate that the paleo-fires prevailed in the southern NCP during the middle

Changhsingian-early Induan and reach their peak near the P–T boundary. This increasing frequency of continental paleo-fires appears to be a global phenomenon, with similar records recorded in other parts of NCP as well as in South China, Australia, and Canada (e.g., Wang and Chen, 2001; Grasby et al., 2011; Shen et al., 2011; Chu et al., 2020).

Factors affecting wildfire include availability of combustible fuel, atmospheric oxygen concentration to enable burning, a suitable climate lacking high moisture, and an ignition mechanism (Scott, 2000). The Zechstein-type flora present across the NCP during the Changhsingian was adapted for dry climates and would have been an appropriate source of fuel. Atmospheric oxygen concentration at the end-Permian has been estimated as 21–27 %, far in excess of the minimum oxygen requirement of 15% for plant combustion (Glasspool and Scott, 2010). Dry and hot climates favor the prevalence of wildfires, and water limited conditions persisted during the Changhsingian in the study area prior to the EMPE (Fig. 7h). However, at the beginning of the EPME interval, the climate tended to be relatively humid reducing the likelihood of wildfire. Therefore, the prevalence of wildfire in the late Changhsingian may have been controlled by ignition factors. Under natural conditions, ignition is caused by lightning, volcanic eruption and less probably meteor impact (Glasspool et al., 2015). Of these, there is no volcanic activity in proximity to the Yuzhou coalfield suitable to ignite wildfires, nor is there any evidence for meteor impact as an ignition mechanism at this time. Lightning would have been the main ignition source of wildfire in the run-up to the EPME, the occurrence of which was related to the climate and atmospheric pCO_2 (Glasspool and Scott, 2010; Glasspool et al., 2015).

In the NCP, wildfire may be the direct cause for both the destruction of terrestrial ecosystems and the rapid decline of plant biodiversity at the EPME, also playing an important role in the extinction of marine organisms (Shen et al., 2011; Zhang et al., 2016). Damage to the land surface vegetation system by frequent wildfire during the EPME interval would have led to increased soil erosion as well as exposing bedrock and increasing continental weathering leading to siltation (Shen et al., 2011).

In the study area, many greyish-green and purplish red mudstone clastics occur in the lake mudstone associated with the CIE-II and persist into the early Triassic in the drill core ZK21-1 (Fig. 8a). This is a common phenomenon in the NCP and similar mudstone clastics also was observed in the uppermost Sunjiagou Formation in borehole core profile in the Liujiang area in Hebei province (middle NCP) (Fig. 8b), and the Shuiyuguan section in Shaanxi Province (middle NCP) (Fig. 8c, d). These mudstone clastics may indicate the increased soil erosion after the collapse of terrestrial vegetation systems. This increased soil erosion does not have a significant effect on the chemical weathering, because it promoted erosion and transportation of the surface soil. However, the decline in CIA values following the EPPE may reflect loss of weathered soils through physical erosion (Cao et al., 2019).

As a result of wildfire, large amounts of organic matter (including charcoal and un-charred matter) and nutrients (including phosphorus and potassium) produced by plant combustion and weathering of parent rock would enter the oceans through surface runoff (Algeo et al., 2013; Glasspool et al., 2015). These inert organic particles would float in ocean for some time, increasing oceanic turbidity through siltation, and affect the penetration of light and the photosynthesis of marine organisms (Glasspool et al., 2015). Large nutrient inputs may be one of the main reasons for prospering cyanobacteria and algae in oceanic surface waters (Meyer et al., 2011; Shen et al., 2015). Eutrophication of seawater during the P-T transition was considered as a localized phenomenon (Algeo et al., 2013) while Sun et al. (2019) considered the transformation of nitrogen to ammonium the main reason for the cyanobacterial proliferation at this time. In this context, oxygen circulation between seawater and atmosphere would have been inhibited by floating inert organic particles, cyanobacteria and algae in surface waters, increasing the consumption of dissolved oxygen by the decomposition of dead cyanobacteria and algae remains (e.g., Algeo et al., 2013; Glasspool et al., 2015; Sun et al., 2019). This would have further contributed to oceanic anoxia and the extinction of aerobic marine organisms.

While siltation may be a causal mechanism for mass extinctions in the marine realm, Wignall et al. (2020) concluded this was not the case for the EPME in the western Guizhou and eastern Yunnan region of the South China Plate (SCP). Plant material in that region was trapped in alluvial settings during base-level rise and did not enter the ocean. However, siltation may have occurred in the southeastern sea area of the NCP. Here fluvial depositional systems, represented by the Jindoushan Sandstone developed through nearly the whole NCP during the P-T transition period following rapid uplift of the IMU to the north (Shang, 1997; Zhang et al., 2014). Large amount of sediment including organic matter may have entered the ocean from the southeast exit of the basin. Sedimentological evidence for this likely siltation is not available because sedimentary strata to the west of the Tanlu Fault (Fig. 1b, c) that would have recorded this were eroded post-deposition.

6. Conclusions

1) Values of $\delta^{13}C_{org}$ show negative excursions in the middle (CIE-I) and end (CIE-II) Changhsingian, the latter roughly corresponds to End-Permian plant extinction (EPPE) in NCP through the comparison of continental weathering trend. We infer CIE-II to be the global negative excursion associated with the EPME, because it occurs in the Meishan and other sections globally, and is synchronous with peaks in nickel concentration and Ni/Al ratio and with the EPPE.

2) Two short-duration episodes with greater humidity, corresponding to CIE-I and CIE-II occurred in the context of the prevailing arid climate from the Changhsingian to the early Induan, inferred from the low kaolinite content and weak continental weathering. The extremely high fusinite content of kerogen macerals and their vertically increasing trend indicates that frequent wildfires occurred in the run up the end Permian. Widespread and frequent wildfire is likely to have been a causal mechanism for the destruction of terrestrial vegetation and ecosystems at the EPME. The appearance of the mudstone clastics coincident with the CIE-II may indicate the increased soil erosion after the collapse of land vegetation systems. The mudstone color shift to green may

indicated the development of less drained alluvial landscapes (e.g., more persistently wet), this is consistent with the change in CIA values.

Acknowledgments

We thank Chu Daoliang for discussion, Sun Yadong, Donald Porcelli, Tamsin Mather, Stephen Grasby and Tracy D. Frank for constructive and helpful reviews of the manuscript. Financial support was provided from the National Natural Science Foundation of China (Grant no. 41472131, 41772161), NERC (NE/P013724/1), National Science and Technology Major Project (Award no. 2017ZX05009-002), and New Century Excellent Talents Fund of Chinese Ministry of Education (Award no. 2013102050020).

References

Algeo, T.J., Henderson, C.M., Tong, J.N., Feng, Q.L., Yin, H.F., Tyson, R.V., 2013. Plankton and productivity during the Permian-Triassic boundary crisis: An analysis of organic carbon fluxes. Glob. Planet. Change 105, 52–67. https://doi.org/10.1016/j.gloplacha.2012.02.008

Algeo, T.J., Twitchett, R.J., 2010. Anomalous early Triassic sediment fluxes due to elevated weathering rates and their biological consequences. Geology 38, 1023–1026. https://doi.org/10.1130/G31203.1

Bachmann, G.H., Kozur, H.W., 2004. The Germanic Triassic: correlations with the international chronostratigraphic scale, numerical ages and Milankovitch cyclicity. Hallersches Jahrb. Geowiss. 26, 17–62.

Bhatia, M.R., Taylor, S.R., 1981. Trace-element geochemistry and sedimentary provinces: A study from the Tasman Geosyncline, Australia. Chem. Geol. 33, 115–125. https://doi.org/10.1016/0009-2541(81)90089-9

Bond, D.P.G., Grasby, S.E., 2017. On the causes of mass extinctions. Palaeogeogr. Palaeoclimatol. Palaeoecol. 478, 3–29. https://doi.org/10.1016/j.palaeo.2016.11.005

Burgess, S.D., Bowring, S.A., 2015. High-precision geochronology confirms voluminous magmatism before, during, and after Earth’s most severe extinction. Sci. Adv. 1. https://doi.org/10.1126/sciadv.1500470

Cao, C.Q., Love, G.D., Hays, L.E., Wang, W., Shen, S.Z., Summons, R.E., 2009. Biogeochemical evidence for euxinic oceans and ecological disturbance presaging the end-Permian mass extinction event. Earth Planet. Sci. Lett. 281, 188–201. https://doi.org/10.1016/j.epsl.2009.02.012

Cao, Y., Song, H.Y., Algeo, T.J., Chu, D.L., Du, Y., Tian, L., Wang, Y.H., Tong, J.N., 2019. Intensified chemical weathering during the Permian-Triassic transition recorded in terrestrial and marine successions. Palaeogeogr. Palaeoclimatol. Palaeoecol. 519, 166–177. https://doi.org/10.1016/j.palaeo.2018.06.012

Chamley, H., 1989. Clay mineralogy. Springer, Berlin, pp. 623.

Chu, D.L., Grasby, S.E., Song, H.J., Dal Corso, J., Wang, Y., Mather, T.A., Wu, Y., Song, H.Y., Shu, W.C., Tong, J.N., Wignall, P.B., 2020. Ecological disturbance in tropical peatlands prior to marine Permian-Triassic mass extinction. Geology 48, 288–292. https://doi.org/10.1130/g46631.1

Chu, D.L., Tong, J.N., Benton, M.J., Yu, J.X., Huang, Y.F., 2019. Mixed continental-marine biotas following the Permian-Triassic mass extinction in South and North China. Palaeogeogr. Palaeoclimatol. Palaeoecol. 519, 95–107. https://doi.org/10.1016/j.palaeo.2017.10.028

Chu, D.L., Tong, J.N., Bottjer, D.J., Song, H.J., Song, H.Y., Benton, M.J., Tian, L., Guo, W.W., 2017. Microbial mats in the terrestrial Lower Triassic of North China and implications for the Permian–Triassic mass extinction. Palaeogeogr. Palaeoclimatol. Palaeoecol. 474, 214–231. https://doi.org/10.1016/j.palaeo.2016.06.013

Chu, D.L., Tong, J.N., Song, H.J., Benton, M.J., Bottjer, D.J., Song, H.Y., Tian, L., 2015. Early Triassic wrinkle structures on land: Stressed environments and oases for life. Sci. Rep. 5, 1–8. https://doi.org/10.1038/srep10109

Cope, T., Ritts, B.D., Darby, B.J., Fildani, A., Graham, S.A., 2005. Late Paleozoic sedimentation on the northern margin of the North China Block: Implications for regional tectonics and climate change. Int. Geol. Rev. 47, 270–296. https://doi.org/10.2747/0020-6814.47.3.270

Dickinson, W.R., 1985. Interpreting provenance relations from detrital modes of sandstones. Proven. arenites. Proc. Cetraro, Cosenza, 1984. https://doi.org/10.1007/978-94-017-2809-6_15

Dong, Y.P., Santosh, M., 2016. Tectonic architecture and multiple orogeny of the Qinling Orogenic Belt, Central China. Gondwana Res. 29, 1–40. https://doi.org/10.1016/j.gr.2015.06.009

Ernst, R.E., Youbi, N., 2017. How Large Igneous Provinces affect global climate, sometimes cause mass extinctions, and represent natural markers in the geological record. Palaeogeogr. Palaeoclimatol. Palaeoecol. 478, 30–52. https://doi.org/10.1016/j.palaeo.2017.03.014

Fedo, C.M., Nesbitt, H.W., Young, G.M., 1995. Unraveling the effects of potassium metasomatism in sedimentary-rocks and paleosols, with implications for paleoweathering conditions and provenance. Geology 23, 921–924. https://doi.org/10.1130/0091-7613(1995)023<0921

Feng, Z., Wei, H.B., Guo, Y., He, X.Y., Sui, Q., Zhou, Y., Liu, H.Y., Gou, X.D., Lv, Y., 2020. From rainforest to herbland: New insights into land plant responses to the end-Permian mass extinction. Earth-Science Rev. 204, 103153. https://doi.org/10.1016/j.earscirev.2020.103153

Fielding, C.R., Frank, T.D., McLoughlin, S., Vajda, V., Mays, C., Tevyaw, A.P., Winguth, A., Winguth, C., Nicoll, R.S., Bocking, M., Crowley, J.L., 2019. Age and pattern of the southern high-latitude continental end-Permian extinction constrained by multiproxy analysis. Nat. Commun. 10, 385. https://doi.org/10.1038/s41467-018-07934-z

Gastaldo, R.A., Kamo, S.L., Neveling, J., Geissman, J.W., Looy, C. V., Martini, A.M., 2020. The base of the Lystrosaurus Assemblage Zone, Karoo Basin, predates the end-Permian marine extinction. Nat. Commun. 11, 1–8. https://doi.org/10.1038/s41467-020-15243-7

Glasspool, I.J., Scott, A.C., 2010. Phanerozoic concentrations of atmospheric oxygen reconstructed from sedimentary charcoal. Nat. Geosci. 3, 627–630. https://doi.org/10.1038/ngeo923

Glasspool, I.J., Scott, A.C., Waltham, D., Pronina, N., Shao, L.Y., 2015. The impact of fire on the late Paleozoic Earth System. Front. Plant Sci. 6, 1–13. https://doi.org/10.3389/fpls.2015.00756

Grasby, S.E., Beauchamp, B., Bond, D.P.G., Wignall, P., Talavera, C., Galloway, J.M., Piepjohn, K., Reinhardt, L., Blomeier, D., 2015. Progressive environmental deterioration in northwestern Pangea leading to the latest Permian extinction. Geol. Soc. Am. Bull. 127, 1331–1347. https://doi.org/10.1130/B31197.1

Grasby, S.E., Beauchamp, B., 2009. Latest Permian to Early Triassic basin-to-shelf anoxia in the Sverdrup Basin, Arctic Canada. Chem. Geol. 264, 232–246. https://doi.org/10.1016/j.chemgeo.2009.03.009

Grasby, S.E., Beauchamp, B., Knies, J., 2016a. Early Triassic productivity crises delayed recovery from world's worst mass extinction. Geology 44, 779–782. https://doi.org/10.1130/G38141.1

Grasby, S.E., Beauchamp, B., Bond, D.P.G., Wignall, P.B., Sanet, H., 2016b. Mercury anomalies associated with three extinction events (Capitanian Crisis, Latest Permian Extinction and the Smithian/Spathian Extinction) in NW Pangea. Geol. Mag. 153, 285–297. https://doi.org/10.1017/S0016756815000436

Grasby, S.E., Sanei, H., Beauchamp, B., 2011. Catastrophic dispersion of coal fly ash into oceans during the latest Permian extinction. Nat. Geosci. 4, 104–107. https://doi.org/10.1038/ngeo1069

Grasby, S.E., Sanei, H., Beauchamp, B., Chen, Z.H., 2013. Mercury deposition through the Permo-Triassic Biotic Crisis. Chem. Geol. 351, 209–216. https://doi.org/10.1016/j.chemgeo.2013.05.022

Grasby, S.E, Knies, J., Beauchamp, B., Bond, D.P.G., Wignall, P.B., Sun, Y.D., 2019a. Global warming leads to Early Triassic nutrient stress across northern Pangea. GSA Bull.

https://doi.org/10.1130/B32036.1

Grasby, S.E., Them, T.R., Chen, Z.H., Yin, R.S., Ardakani, O.H., 2019b. Mercury as a proxy for volcanic emissions in the geologic record. Earth-Science Rev. 196, 102880. https://doi.org/10.1016/j.earscirev.2019.102880

Guo, X.N., Tang, Z.L., Li, W.C., Sheng, J.H., Gao, Y.S., Sun, J.P., Wei, H.X., Ren, J.K., Yang, J.Y., Li, T.L., Li, H.W., Qiu, G.B., Liang, X.Y., Song, J.J., Guan, Z.M., Li, Y.J., Song, Z.J., Su, X.B., 1991. The late Palaeozoic coal-accumulating laws in Henan province. China University of Geoscience Press,Wuhan, pp. 51-61.

Hao, Y.W., Luo, M.S., Xu, Z.L., Zou, Y.R., Tang, T.T., 2014. Division of sedimentary basina and its tectonic evolution in North China from Newproterozoic to Mesozoic. Earth Sci. China Univ. Geosci. 39, 1230–1242. https://doi.org/10.3799/dqkx.2014.106

Hou, J.P., Ouyang, S., 2000. Palynoflora from the Sunjiagou Formation in Liulin County, Shanxi Province. Acta Palaeontol. Sin. 39, 356–368.

Hu, F.Z., Fu, X.G., Lin, L., Song, C.Y., Wang, Z.W., Tian, K.Z., 2020. Marine Late Triassic-Jurassic carbon-isotope excursion and biological extinction records: New evidence from the Qiangtang Basin, eastern Tethys. Glob. Planet. Change 185, 103093. https://doi.org/10.1016/j.gloplacha.2019.103093

Joachimski, M.M., Lai, X., Shen, S., Jiang, H., Luo, G., Chen, B., Chen, J., Sun, Y., 2012. Climate warming in the latest Permian and the Permian-Triassic mass extinction. Geology 40, 195–198. https://doi.org/10.1130/G32707.1

Li, J.Y., 2006. Permian geodynamic setting of Northeast China and adjacent regions: closure of the Paleo-Asian Ocean and subduction of the Paleo-Pacific Plate. J. Asian Earth Sci. 26, 207–224.

https://doi.org/10.1016/j.jseaes.2005.09.001

Liao, Z.W., Hu, W.X., Cao, J., Wang, X.L., Fu, X.G., 2020. Oceanic anoxia through the late Permian Changhsingian stage in the Lower Yangtze region, South China: Evidence from sulfur isotopes and trace elements. Chem. Geol. 532, 119371. https://doi.org/10.1016/j.chemgeo.2019.119371

Liao, Z.W., Hu, W.X., Cao, J., Wang, X.L., Yao, S.P., Wu. H.G., Wan, Y., 2016. Permian-Triassic boundary (PTB) in the Lower Yangtze Region, southeastern China: A new discovery of deep-water archive based on organic carbon isotopic and U-Pb geochronological studies. Palaeogeogr. Palaeoclimatol. Palaeoecol. 451, 124–139. https://doi.org/10.1016/j.palaeo.2016.03.004

Ma, P.F., Wang, L.C., Wang, C.S., Wu, X.H., Wei, Y.S., 2015. Organic-matter accumulation of the lacustrine Lunpola oil shale, central Tibetan plateau: Controlled by the paleoclimate, provenance, and drainage system. Int. J. Coal Geol., 147-148, 58–70. https://doi.org/ 10.1016/j.coal.2015.06.011

Meyer, K.M., Yu, M., Jost, A.B., Kelley, B.M., Payne, J.L., 2011. $\delta^{13}C$ evidence that high primary productivity delayed recovery from end-Permian mass extinction. Earth Planet. Sci. Lett. 302, 378–384. https://doi.org/10.1016/j.epsl.2010.12.033

Muttoni, G., Gaetani, M., Kent, D.V., Sciunnach, D., Angiolini, L., Berra, F., Garzanti, E., Mattei, M., Zanchi, A., 2009. Opening of the Neo-tethys ocean and the Pangea B to Pangea A transformation during the permian. GeoArabia 14, 17–48. https://doi.org/10.1016/S0012-821X(03)00452-7

Nan, J.Y., Li, Y.Y., 2004. organic and inorganic carbon-isotope shift and paleoenvironment at the P-T boundary section in Meishan. Geochimica 33, 9–19.

https://doi.org/10.3321/j.issn:0379-1726.2004.01.002

Nesbitt, H.W., Young, G.M., 1984. Prediction of some weathering trends of plutonic and volcanic rocks based on thermodynamic and kinetic considerations. Geochim. Cosmochim. Acta 48, 1523–1534. https://doi.org/10.1016/0016-7037(84)90408-3

Pan, Z.C., Xu, L., Xi, Y.H., Jia, S.H., 2008. Research on stratigraphic paleontology in Henan province−The Mesozoic. Zhenghou: The Yellow River Water Conservancy Press. Zhengzhou, pp. 3-33.

Rampino, M.R., Rodriguez, S., Baransky, E., Cai, Y., 2017. Global nickel anomaly links Siberian Traps eruptions and the latest Permian mass extinction. Sci. Rep. 7, 12416. https://doi.org/10.1038/s41598-017-12759-9

Ren, J.S., 1987. Geotectonic evolution of China. Springer.

Retallack, G.J., 2013. Ediacaran gaskiers glaciation of newfoundland reconsidered. J. Geol. Soc. London. 170, 19–36. https://doi.org/10.1144/jgs2012-060

Roy, D.K., Roser, B.P., 2013. Climatic control on the composition of Carboniferous-Permian Gondwana sediments, Khalaspir basin, Bangladesh. Gondwana Res. 23, 1163–1171. https://doi.org/10.1016/j.gr.2012.07.006

Sanei, H., Grasby, S.E., Beauchamp, B., 2012. Latest Permian mercury anomalies. Geology 40, 63–66. https://doi.org/10.1130/G32596.1

Scott, A.C., 2000. The Pre-Quaternary history of fire. Palaeogeogr. Palaeoclimatol. Palaeoecol. 164, 281–329. https://doi.org/10.1016/S0031-0182(00)00192-9

Shang, G.X., 1997. The late Paleozoic coal geology of North China Platform, Taiyuan: Shanxi Science and Technology Press, Taiyuan, pp. 1-160.

Shen, J., Algeo, T.J., Hu, Q., Zhang, N., Zhou, L., Xia, W.C., Xie, S.C., Feng, Q.L., 2012. Negative C-isotope excursions at the Permian-Triassic boundary linked to volcanism. Geology 40, 963–966. https://doi.org/10.1130/G33329.1

Shen, J., Schoepfer, S.D., Feng, Q.L., Zhou, L., Yu, J.X., Song, H.Y., Wei, H.Y., Algeo, T.J., 2015. Marine productivity changes during the end-Permian crisis and Early Triassic recovery. Earth-Science Rev. 149, 136–162. https://doi.org/10.1016/j.earscirev.2014.11.002

Shen, J., Yu, J.X., Chen, J.B., Algeo, T.J., Xu, G.Z., Feng, Q.L., Shi, X., Planavsky, N.J., Shu, W.C., Xie, S.C., 2019. Mercury evidence of intense volcanic effects on land during the permian-triassic transition. Geology 47, 1117–1121. https://doi.org/10.1130/G46679.1

Shen, S.Z., Cao, C.Q., Zhang, H., Bowring, S.A., Henderson, C.M., Payne, J.L., Davydov, V.I., Chen, B., Yuan, D.X., Zhang, Y.C., Wang, W., Zheng, Q.F., 2013. High-resolution $\delta^{13}C_{carb}$ chemostratigraphy from latest Guadalupian through earliest Triassic in South China and Iran. Earth Planet. Sci. Lett. 375, 156–165. https://doi.org/10.1016/j.epsl.2013.05.020

Shen, S.Z., Crowley, J.L., Wang, Y., Bowring, S.A., Erwin, D.H., Sadler, P.M., Cao, C.Q., Rothman, D.H., Henderson, C.M., Ramezani, J., Zhang, H., Shen, Y., Wang, X.D., Wang, W., Mu, L., Li, W.Z., Tang, Y.G., Liu, X.L., Liu, L.J., Zeng, Y., Jiang, Y.F., Jin, Y.G., 2011. Calibrating the end-Permian mass extinction. Science 334, 1367–1372. https://doi.org/10.1126/science.1213454

Shen, S.Z., Zhang, H., Zhang, Y.C, Yuan, D.X., Chen, B., He, W.H., Mu, L., Lin, W., Wang, W.Q., Chen, J., Wu, Q., Cao, C.Q., Wang, Y., Wang, X.D., 2019. Permian integrative stratigraphy and timescale of China. Sci. China Earth Sci. 62, 154–188. https://doi.org/10.1007/s11430-017-9228-4

Sun, H., Xiao, Y.L., Gao, Y.J., Zhang, G.J., Casey, J.F., Shen, Y.N., 2018. Rapid enhancement of chemical weathering recorded by extremely light seawater lithium isotopes at the Permian-Triassic boundary. Proc. Natl. Acad. Sci. U. S. A. 115, 3782–3787. https://doi.org/10.1073/pnas.1711862115

Sun, Y.D., Joachimski, M.M., Wignall, P.B., Yan, C.B., Chen, Y.L., Jiang, H.S., Wang, L.N., Lai, X.L., 2012. Lethally hot temperatures during the early triassic greenhouse. Science 338, 366–370. https://doi.org/10.1126/science.1224126

Sun, Y.D., Wignall, P.B., Joachimski, M.M., Bond, D.P.G., Grasby, S.E., Lai, X.L., Wang, L.N., Zhang, Z.T., Sun, S., 2016. Climate warming, euxinia and carbon isotope perturbations during the Carnian (Triassic) Crisis in South China. Earth Planet. Sci. Lett. 444, 88–100. https://doi.org/10.1016/j.epsl.2016.03.037

Sun, Y.D., Zulla, M.J., Joachimski, M.M., Bond, D.P.G., Wignall, P.B., Zhang, Z.T., Zhang, M.H., 2019. Ammonium ocean following the end-Permian mass extinction. Earth Planet. Sci. Lett. 518, 211–222. https://doi.org/10.1016/j.epsl.2019.04.036

Thiry, M., 2000. Palaeoclimatic interpretation of clay minerals in marine deposits: An outlook from the continental origin. Earth Sci. Rev. 49, 201–221. https://doi.org/10.1016/S0012-8252(99)00054-9

Van Soelen, E.E., Twitchett, R.J., Kürschner, W.M., 2018. Salinity changes and anoxia resulting from enhanced run-off during the late Permian global warming and mass extinction event. Clim. Past 14, 441–453. https://doi.org/10.5194/cp-14-441-2018

Wang, R.N., 1997. New Advance of the Study of the Shiqianfeng Formation in Western Henan. Geol. Rev. 43, 200–209.

Wang, Z.Q., Chen, A. S., 2001. Traces of arborescent lycopsids and dieback of the forest vegetation in relation to the terminal Permian mass extinction in North China. Rev. Palaeobot. Palynol. 117, 217–243. https://doi.org/10.1016/S0034-6667(01)00094-X

Wang, Z.Q, Wang, L., 1986. Late Permian fossil plants from the lower part of the Shiqianfeng (Shihchienfeng) group in North China. Bull. Tianjin Inst. Geol.Min.Res.No. 15, 1–80.

Wignall, P.B., Chu, D.L., Hilton, J., Dal Corso, J., Wu, Y.Y., Wang, Y., Atkinson, J., Tong, J.N. 2020. Death in the Shallows: the record of Permo-Triassic mass extinction in paralic settings, southwest China. Glob. Planet. Change https://doi.org/10.1016/j.gloplacha.2020.103176.

Wignall, P.B., Hallam, A., 1992. Anoxia as a cause of the Permian/Triassic mass extinction: facies evidence from northern Italy and the western United States. Palaeogeogr. Palaeoclimatol. Palaeoecol. 93, 21–46. https://doi.org/10.1016/0031-0182(92)90182-5

Wignall, P.B., Twitchett, R.J., 1996. Oceanic Anoxia and the End Permian Mass Extinction. Science 272, 1155–1158. https://doi.org/10.1126/science.272.5265.1155

Winguth, A., Winguth, C., 2013. Precession-driven monsoon variability at the Permian-Triassic boundary - Implications for anoxia and the mass extinction. Glob. Planet. Change 105, 160–170. https://doi.org/10.1016/j.gloplacha.2012.06.006

Wu, Y., Fan, T.L., Jiang, S., Yang, X.Q., 2017. Lithofacies and sedimentary sequence of the lower Cambrian Niutitang shale in the upper Yangtze platform, South China. J. Nat. Gas Sci. Eng. 43, 124–136. https://doi.org/10.1016/j.jngse.2017.04.002

Xie, S.C., Pancost, R.D., Huang, J.H., Wignall, P.B., Yu, J.X., Tang, X.Y., Chen, L., Huang, X.Y., Lai, X.L., 2007. Changes in the global carbon cycle occurred as two episodes during the Permian-Triassic crisis. Geology 35, 1083–1086. https://doi.org/10.1130/G24224A.1

Yang, G.X., Wang, H.S., 2012. Yuzhou Flora-A hidden gem of the Middle and Late Cathaysian

Flora. Sci. China Earth Sci. 55, 1601–1619. https://doi.org/10.1007/s11430-012-4476-2

Yang, Q., Lei, S., 1987. Depositional Environments and Coal-forming Characteristics of Late Palaeozoic Coal Measures in Yuxian, Henan Province, Beijing: Geological Publishing House.

Yin, H.F., Song, H.J., 2013. Mass extinction and Pangea integration during the Paleozoic-Mesozoic transition. Sci. China Earth Sci. 56, 1791–1803. https://doi.org/10.1007/s11430-013-4624-3

Zhang, G.W., Meng, Q.R., Lai, S.C., 1995. Tectonics and structure of Qinling orogenic belt. Sci. China Chem. 38, 1379–1394. https://doi.org/10.1007/BF00696740

Zhang, H., Cao, C.Q., Liu, X.L., Mu, L., Zheng, Q.F., Liu, F., Xiang, L., Liu, L.J., Shen, S.Z., 2016. The terrestrial end-Permian mass extinction in South China. Palaeogeogr. Palaeoclimatol. Palaeoecol. 448, 108–124. https://doi.org/10.1016/j.palaeo.2015.07.002

Zhao, Y., Zhai, M.G., Chen, H., Zhang, S.H., 2017. Paleozoic-early Jurassic tectonic evolution of North China Craton and its adjacent orogenic belts. Geol. China 44, 44–60. https://doi.org/10.12029/gc20170104

Zhang, S.H., Zhao, Y., Ye, H., Liu, J. M., Hu, Z.C., 2014. Origin and evolution of the Bainaimiao arc belt: Implications for crustal growth in the southern Central Asian orogenic belt. Geol. Soc. Am. Bull. 126, 1275–1300. https://doi.org/10.1130/B31042.1

Ziegler, A.M., Hulver, M.L., Rowley, D.B., 1997. Permian world topography and climate, in: Late Glacial and Postglacial Environmental Changes: Quaternary, Carboniferous-Permian and Proterozoic. Oxford Univ Press, pp. 111–146.

Figure captions

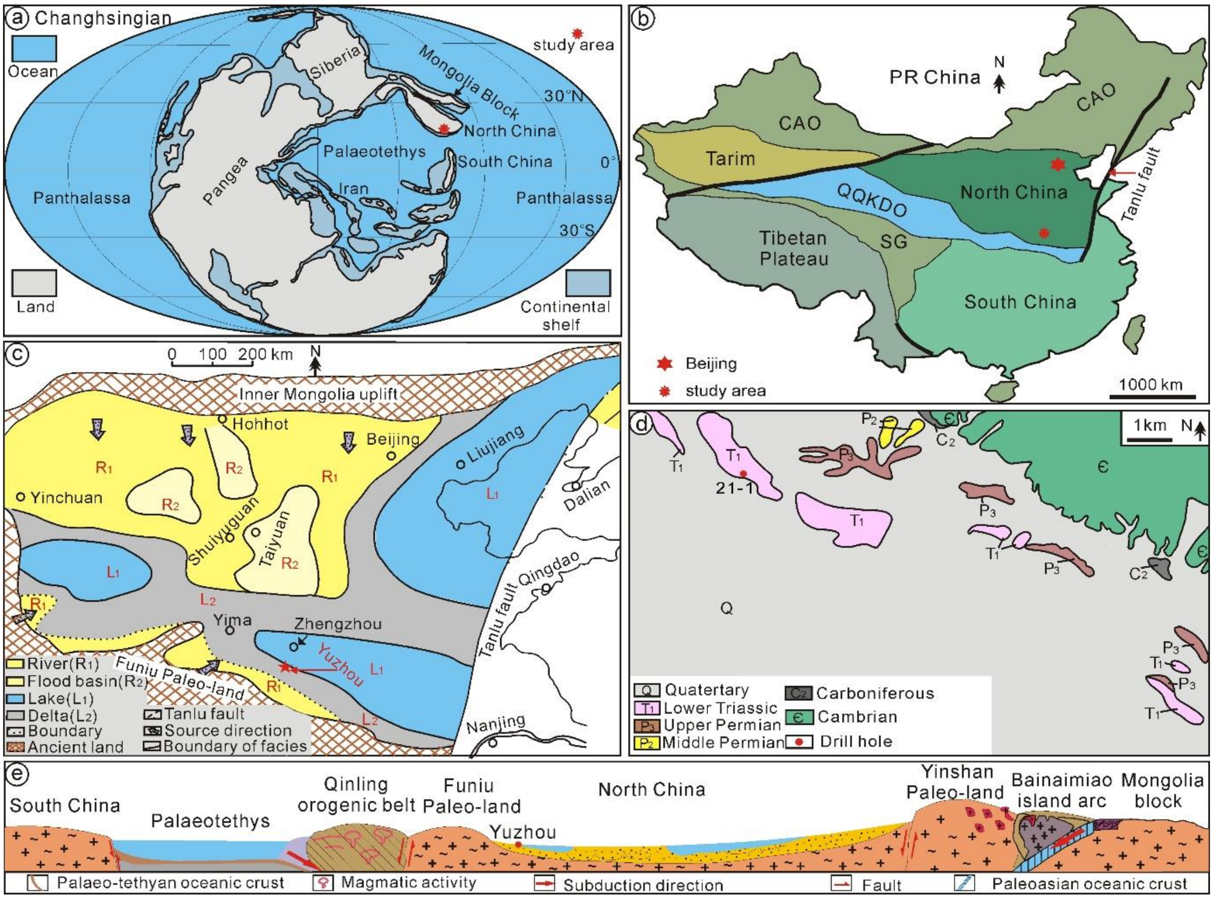

Figure 1. Location and geological context for the study area. **a**, Paleogeographic reconstruction for the Lopingian (late Permian) showing location of North China Plate (modified from Ziegler et al., 1997); **b**, Generalized tectonic map of present-day China showing the location of the North China Plate and the study area (modified from Ren, 1987), Abbreviations: CAO = Central Asian Orogen; SG = Songpan-Ganzi; QQKDO = Qinling-Qilian-Kunlun-Dabie Orogen; **c**, Paleofacies map of the North China Plate during the Changhsingian (Sunjiagou Formation) showing the location of study area (modified from Shang, 1997), Abbreviations: R1= river; L1= lake; L2= delta; **d**, Local geological map of the Yuzhou coalfield showing the locations of the borehole core sections in the study area, Abbreviations: Q=Quaternary; L1=Lower Triassic; P3=Upper Permian; P2=Middle Permian; C2= Carboniferous; Є= Cambrian, and the number represents drill hole number, e.g., 21-1; **e**, Schematic diagram showing the basin-mountain relationships and the location of the North China

Plate during the Lopingian (modified from Shang, 1997; Zhao et al., 2017).

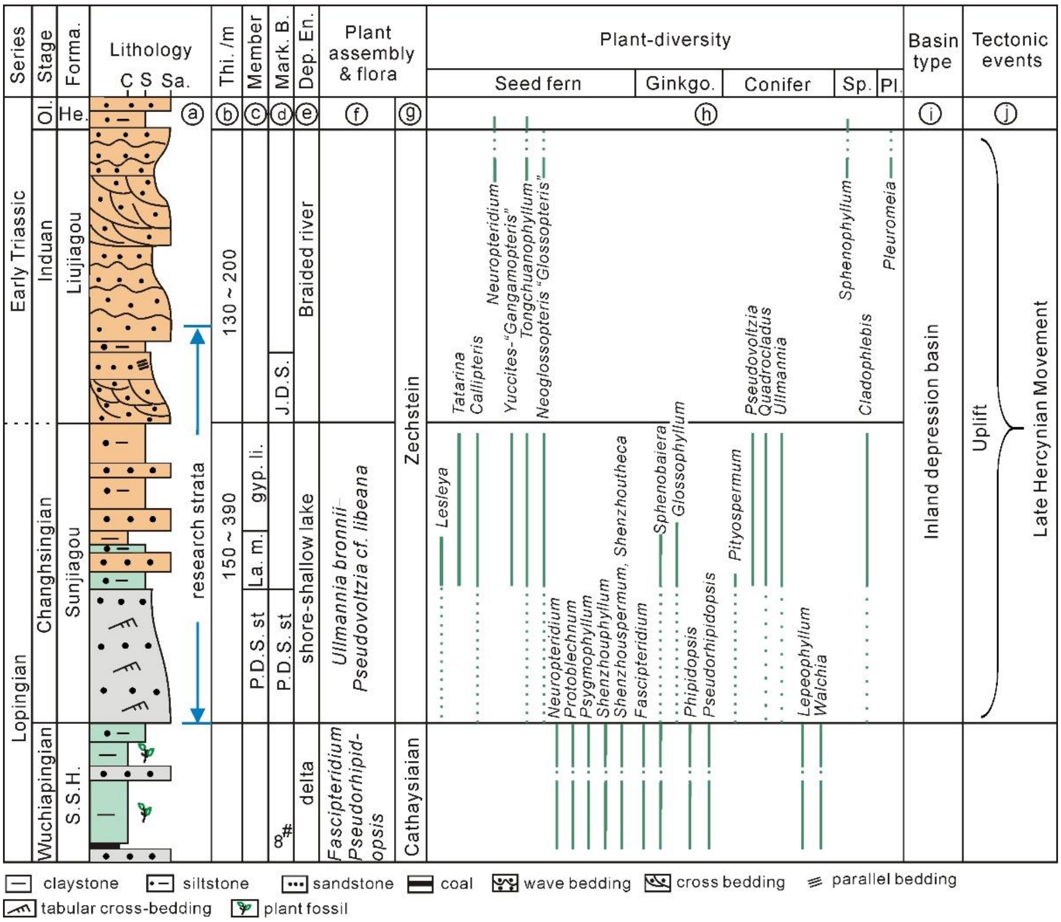

Figure 2. Stratigraphic framework for the Permian-Triassic boundary strata from the Yuzhou coalfield. Note: Lithology from Yang and Lei (1987) and the colors filling in lithology are similar to that of the rocks. **a**, Strata in the basin highlighting the study interval; **b**, Formation thicknesses from Guo et al. (1991) and Pan et al. (2008); **c**, Stratigraphic division of the Sunjiagou Formation from Yang and Lei (1987) and Wang (1997); **d**, Marker beds from Guo et al. (1991); **e**, Summary sedimentary environments from Guo et al. (1991); **f**, Fossil plant assemblages from Yang and Wang (2012); **g**, Floral provinces from Wang and Wang (1986), Pan et al. (2008) and Yang and Wang (2012); **h**, Vertical distribution of plant fossils from Chu et al. (2015) showing the extinction near the boundary of the Sunjiagou and Liujiugou formations; **i**, Basin type from Hao et al. (2014); **j**,

Tectonic events from Shang (1997) and Zhao et al. (2017). Abbreviations: Ol. = Olenekian; Forma. = Formation; He. = Heshanggou; S.S.H. = Shangshihezi; C = Clay; S = Siltstone; Sa. = Sandstone; Thi. = Thick; Mark. B. = Marker bed; $8^{\#}$ = 8# coal seams; P.D.S.st: Pingdingshan sandstone; La. m.: Lamellibranchiate marl; Gyp. Li.: Gypsum lime-nodule; J.D.S.: Jindoushan Sandstone; Dep. En. = Depositional environment; Sporo. = Sporo-pollen; *Ginkgo*.: Ginkgopsida; Sp.: Sphenopsida; Pl.:

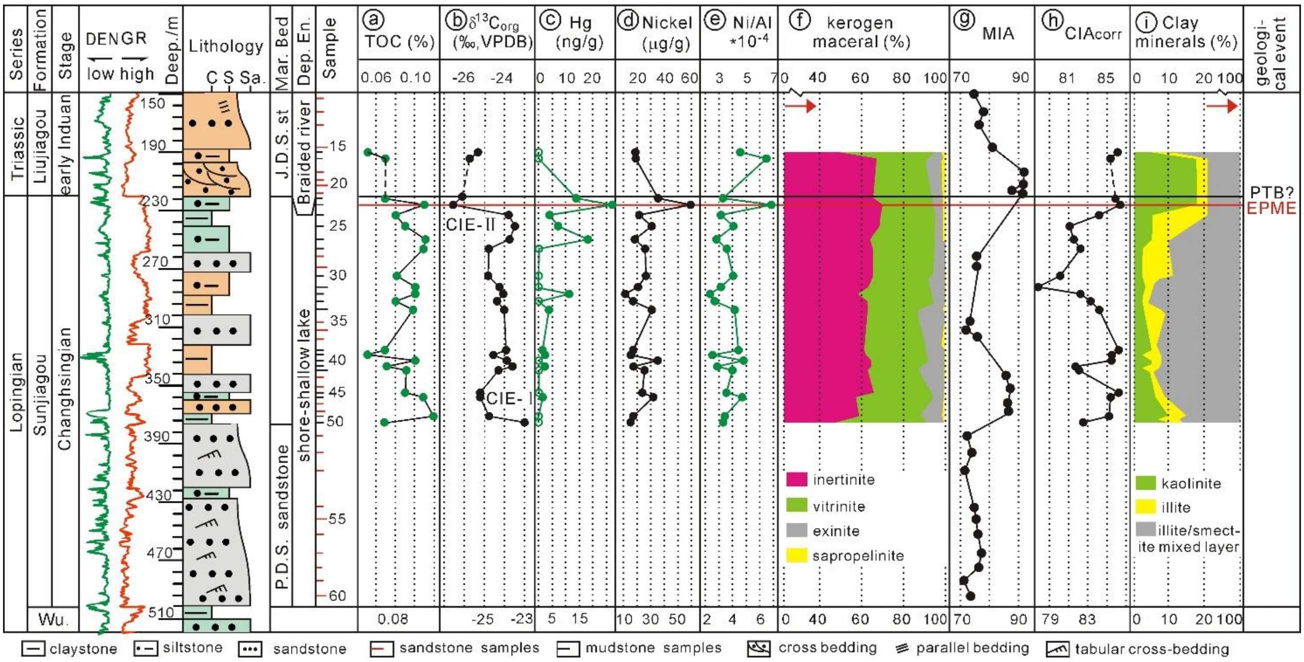

Figure 3. Change in value of TOC, $\delta^{13}C_{org}$, Hg and nickel concentrations, kerogen macerals, MIA and CIA, and clay minerals component in the study area. Note: the colors filling in lithology are similar to that of rocks, the interpretation of the deposition environment is from Guo et al. (1991) and Pan et al. (2008), and pay attention to the scales in column f and i. Abbreviations: C = claystone; S = siltstone; Sa. = sandstone; Mark. Bed = marker bed; Dep. En. = depositional environment; J.D.S st = Jindoushan Sandstone; P.D.S. sandstone = Pingdingshan sandstone; PTB = Permian-Triassic boundary; EPME = End Permian mass extinction.

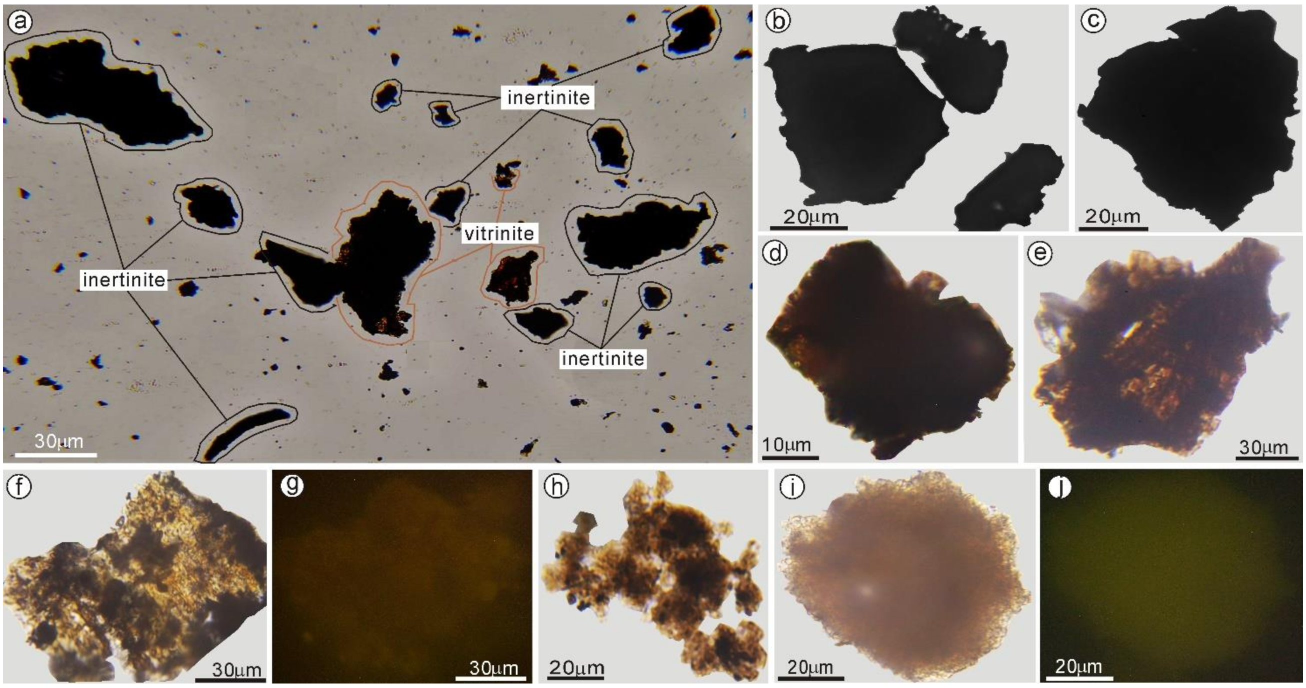

Figure 4. Photomicrographs showing microstructure characteristics of kerogen macerals in the study area. **a**, overview showing characteristics of kerogen macerals (transmitted light, sample #23); **b** and **c**, fusinite (transmitted light, #45); **d** and **e**, vitrinite (transmitted light, sample #16 and #49); **f** and **g**, suberinite (transmitted light and fluorescence, respectively, sample #42); **h**, sapropelinite (transmitted light, sample #22); **i** and **j**, sapropelinite (transmitted light and fluorescence, respectively, sample #50)

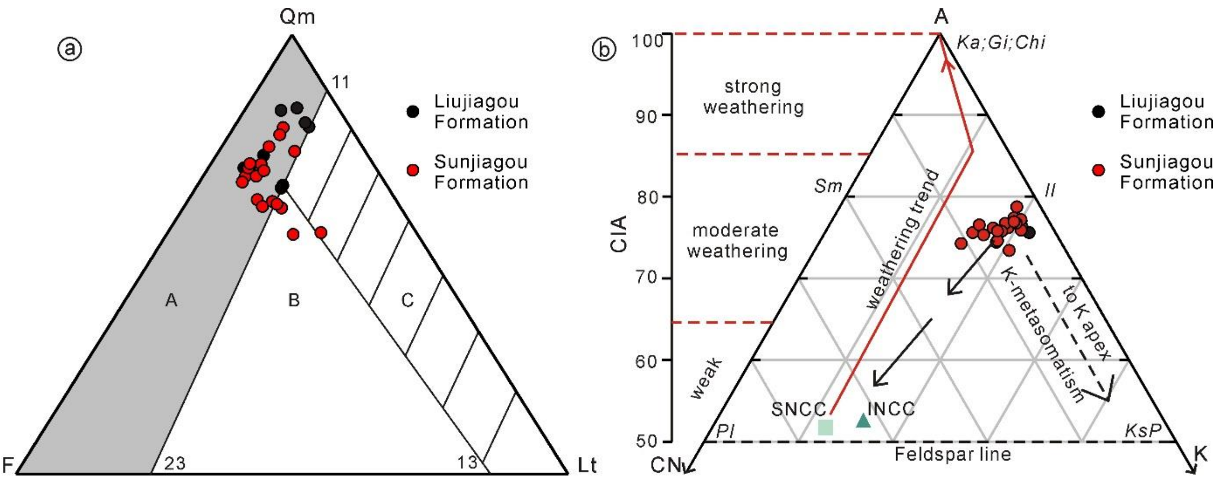

Figure 5. Qm-F-Lt diagram of sandstone and A-CN-K diagram of mudstone in the study area. **a**, Qm-F-Lt diagram of sandstone samples from Changhsingian to early Induan showing the main

provenance area of continental block (modified from Dickinson, 1985). Abbreviations: Qm = monocrystalline quartz; F = feldspar (plagioclase + K-feldspar); Lt = total lithics (lithics + polycrystalline quartz); A = Continental block; B = Magmatic arc; C = Recycled orogen. **b**, A-CN-K diagram of mudstone samples from Changhsingian to early Induan with the chemical index of alteration (CIA) scale to the left, showing the possible influence of Potassium metasomatism. For comparison, the average upper crust CIA value of southern and interior North China Craton are shown (modified from Cao et al., 2019). Abbreviations: A = Al_2O_3; CN = $CaO^{*}+Na_2O$; K = K_2O; CIA= chemical index of alteration; Ka = kaolinite; Gi = gibbsite; Il = illite; PI = Plagioclase; Chl = chlorite; Sm = smectite; Ksp = K-feldspar; INCC = Interior North China Craton; SNCC = Southern North China Craton.

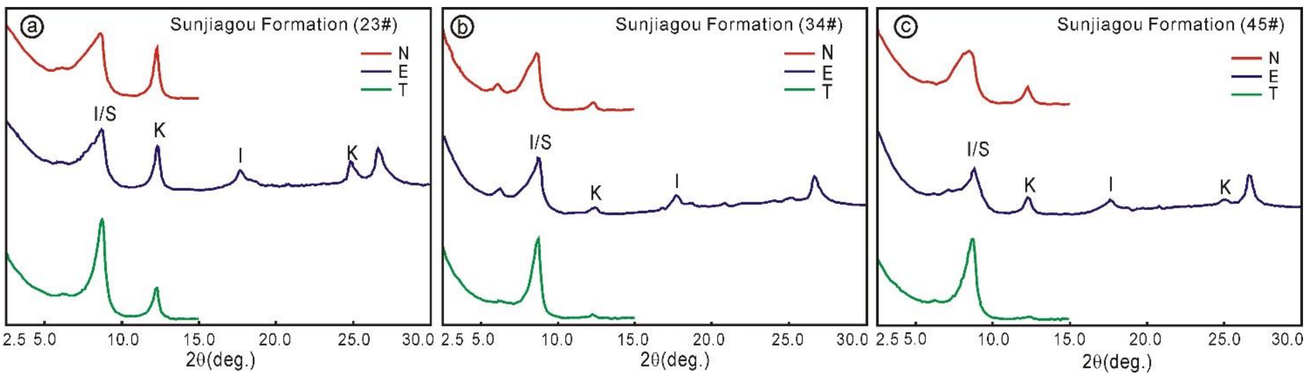

Figure 6. X-ray diffraction (XRD) patterns of clay fractions of typical samples in the study area. N, E and T designate spectra of a naturally-oriented slide, ethylene-glycol saturated for oriented slide and high-temperature treated at 450°C for oriented slide, respectively. **a**, XRD patterns showing high content of illite-smectite mix layer and kaolinite (Sunjiagou Formation, sample #23); **b**, XRD patterns showing high content of illite-smectite mix layer and lowest kaolinite content (Sunjiagou Formation, sample #34); **c**, XRD patterns showing high content of illite-smectite mix layer and less kaolinite content (Sunjiagou Formation, sample #45). Abbreviations: I/S = illite-smectite mixed layer; K = kaolinite; I = illite.

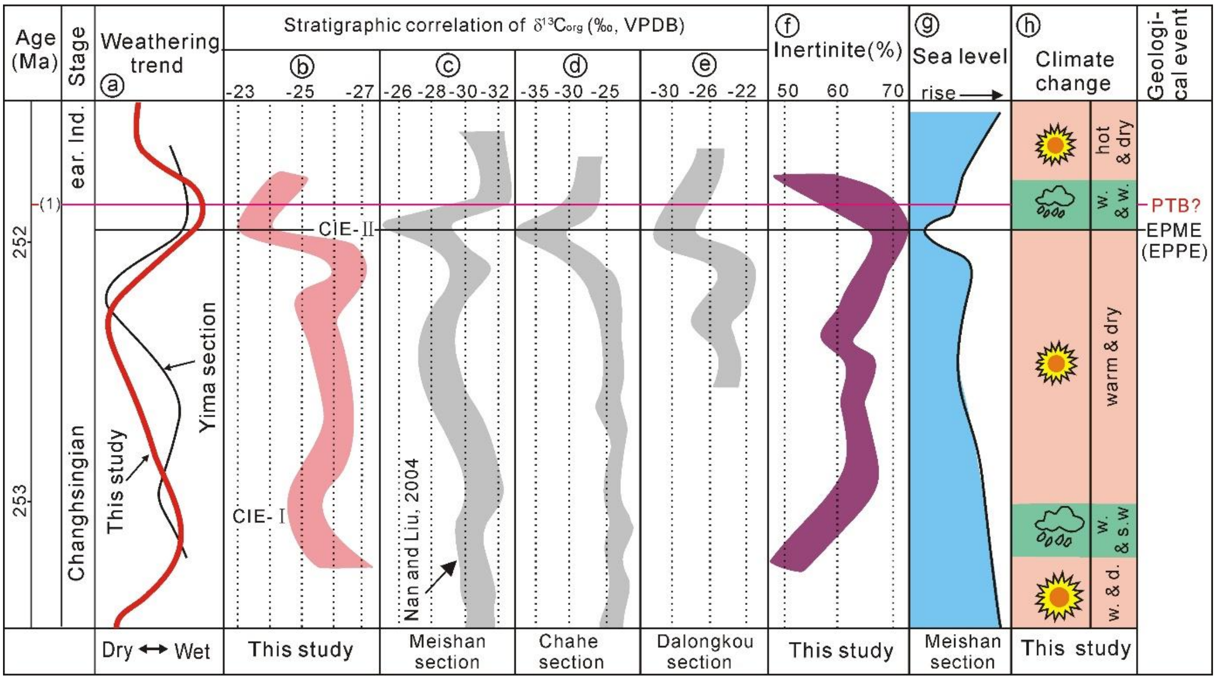

Figure 7. Comparison among weathering trend, carbon isotope records, inertinite content, sea-level, and the paleoenvironment events from Changhsingian to early Induan. Age stratigraphic framework from Shen S. et al. (2019); (1) represents P-T boundary age: 251.902 ± 0.024Ma; **a**, red curve represent a weathering trend by MIA and CIA in the study area, and the black curve represent a weathering trend by CIA in Yima section (southern NCP) near the study area (Cao et al., 2019); **b**, vertical change trend of $\delta^{13}C_{org}$ in the study area showing two negative isotope excursions near the middle and end of the Changhsingian; **c, d** and **e**, $\delta^{13}C_{org}$ from the marine (Meishan) and terrestrial (Chahe and Dalongkou) sections by Nan and Liu (2004), Zhang et al. (2016) and Shen J et al. (2019); **f**, inertinite content from the present study; **g**, sea-level curve (relative to current sea level) of the Meishan section from Cao et al. (2009); **h**, paleoclimate change inferred from clay mineral component, CIA and MIA. Abbreviations: ear. Ind. = early Induan; w. & d. = warm & dry; w. & s. w. = warm & slight wet; w. & w. = warm & wet; PTB = Permian-Triassic boundary; EPME = End Permian mass extinction; EPPE = End Permian plant extinction.

Figure 8. Pictures showing a lot of mudstone clastics was observed in uppermost Sunjiagou Formation in NCP. **a**: lots of greyish-green and purplish-red mudstone clastics occur in the lake mudstone associated with the CIE-II and last into early Triassic in the drill core ZK21-1, Henan province (southern NCP). Note: the colors filling in lithology are similar to that of rocks, and the numbers (e.g.,(1)-(3)) represent the vertical order of lithology. **b**: lots of mudstone clastics was observed in the uppermost Sunjiagou Formation in borehole core profile in Liujiang area, Hebei province (middle NCP). **c**: Picture of Shuiyuguan section (Shaanxi province, middle NCP) showing the boundary of Sunjiagou and Liujiagou formations with highlighted box enlarged in d. **d:** enlargement from c showing details of mudstone clastics in the uppermost Sunjiagou Formation.